RSC Advances

PAPER

View Article Online
View Journal | View Issue

Cite this: *RSC Adv.*, 2026, **16**, 4452

Multifunctional Tm^{3+}/Yb^{3+}:$Na_5Y(MoO_4)_4$ nanocrystals for simultaneous luminescent nanothermometry, photothermal therapy and deep bioimaging in the NIR-I window

Yosra Bahrouni, *[ac] Ikhlas Kachou, [a] Kamel Saidi, *[ab] Christian Hernández-Álvarez, [cd] Mohamed Dammak [a] and I. R. Martin [c]

In this study, Tm^{3+}/Yb^{3+} co-doped $Na_5Y(MoO_4)_4$ (NYMO) nanoparticles were successfully synthesized *via* the sol–gel method, and their structural, morphological, upconversion (UC) luminescence, and photothermal properties were comprehensively investigated. Upon 975 nm near-infrared (NIR) laser excitation, the NYMO nanoparticles exhibited two prominent UC emission bands at 477 nm and 796 nm, corresponding to the $^1G_4 \rightarrow {}^3F_6$ and $^3H_4 \rightarrow {}^3H_6$ transitions of Tm^{3+} ions, respectively. The fluorescence intensity ratio (FIR) between these emissions enabled precise optical temperature sensing; at 298 K, the highest relative sensitivity is 2.05% K^{-1}, and at 388 K, the highest absolute sensitivity is 0.53% K^{-1}. The FIR value increased with excitation power, indicating a rise in internal temperature due to photothermal effects. This temperature increase is attributed to efficient NIR absorption and nonradiative relaxation processes, enhanced by electron–phonon interactions at elevated temperatures. Furthermore, the nanoparticles demonstrated significant NIR emission penetration into biological tissue up to a depth of 4 mm, confirming their suitability for deep-tissue imaging. Operating within the optically transparent biological window, the Tm^{3+}/Yb^{3+}-doped NYMO nanoparticles exhibit multifunctional capabilities, combining optical thermometry, photothermal conversion, and *in vivo* bioimaging. These results highlight NYMO nanoparticles as promising candidates for luminescent nanothermometers and photothermal agents in biomedical applications.

Received 19th November 2025
Accepted 31st December 2025

DOI: 10.1039/d5ra08947f

rsc.li/rsc-advances

1. Introduction

Currently, upconversion luminescence is recognized as a novel process in which two or more low-energy photons are sequentially absorbed, leading to the emission of a photon with higher energy.[1,2] The trivalent rare earth (RE^{3+}) ions exhibit a plethora of ladder-like 4f energy levels, creating optimal physical conditions for upconversion (UC) to transpire. The RE-doped UC materials exhibit several exceptional characteristics. These include a large anti-Stokes shift, precise emission bands, extended luminescence lifetimes and superior photostability, which make them promising materials in various applications such as lasers, illumination, displays, anti-counterfeiting and sensors.[3,4] Upconversion (UC) using a near-infrared (NIR) excitation source has attracted significant attention in the biomedical field due to its favorable characteristics deep penetration into biological tissues and minimal autofluorescence.[5–7] In parallel, photothermal therapy (PTT) is a therapeutic approach that converts absorbed light energy into heat *via* photothermal therapeutic agents (PTAs), enabling efficient destruction of cancer cells or pathogens through thermal ablation.[8,9] The RE upconversion device consists of a host matrix and selected luminescent centers of RE ions, such as Tm^{3+} and Yb^{3+}, for the generation of the desired emission. Sensitizers such as Yb^{3+} or Nd^{3+} are typically used to enhance absorption and improve lasing intensity. Moreover, optimal candidates for upconversion are host materials with low phonon energy and sufficient asymmetric lattice sites to allow substitution of lanthanide ions for luminescence.[10,11] Materials doped with RE^{3+} seem to be a promising alternative for creating optically active materials since the RE^{3+} ions have thermally linked emission levels.[12] It means that the relative ion population of these planes, as well as their emission, varies with the temperature of the active substance.[13,14] Several optical

[a]*Laboratoire de Physique Appliquée, Faculté des Sciences de Sfax, Département de Physique, Université de Sfax, BP 1171 Sfax, Tunisia. E-mail: yossrabahrouni23@gmail.com; saidikamel494@gmail.com*

[b]*University of Sfax, Department of Physics, Sfax Preparatory Engineering Institute, 1172-3000 Sfax, Tunisia*

[c]*Universidad de La Laguna, Departamento de Física, MALTA-Consolider Team, IMN and IUdEA Apdo, Correos 456, E-38206, San Cristóbal de La Laguna, Santa Cruz de Tenerife, Spain*

[d]*Adam Mickiewicz University, Faculty of Chemistry, Uniwersytetu Poznańskiego 8, 61-614 Poznań, Poland*

parameters can be calibrated for studying the RE^{3+} emission response as a function of temperature, including the relative intensities between two thermalized emission bands, commonly known as the fluorescence intensity ratio (FIR), which is the most commonly used technique for calibrating an optical sensor.[15,16] From a practical point of view, not all RE^{3+} ions can be used to calibrate optical responses using the FIR technique.[17]

Among lanthanide elements, Yb^{3+} and Tm^{3+} are considered the most efficient sensitizers, exhibiting strong absorption cross-sections at an excitation wavelength of 975 nm, close to the near-infrared (NIR) band. The order distribution of Yb^{3+} between $^2F_{7/2}$ and $^2F_{5/2}$ is likewise resonant with that of other regularly employed UC lanthanides, which contain only a 4F order of the $^2F_{5/2}$ single excited state.[18,19] Efficient energy conversion is promoted by the f–f transitions of elemental ions (Eu^{3+}, Tm^{3+} and Ho^{3+}). Therefore, Tm^{3+} is a suitable sensitizer for *in vivo* experiments. It may be utilized as an excitation light source, therefore avoiding the thermal damage to biological tissues caused by the 980 nm laser. Yb^{3+} and Tm^{3+} are the most often employed ions for sensitizer conversion owing to their deep tissue penetration ability.[20–22] The activator is responsible for releasing the light from the luminescent substance incorporated in the host matrix. The activator stimulates follow-up and then transitions to a higher energy level, hence minimizing the possibility of non-radiative energy relaxation. The energy dissipation associated with cross-relaxation may be reduced by altering the doping ratios of the various activators to regulate light emission.[23] When excited by a 975 nm laser, the UC emission of a typical activator Tm^{3+} is typically in the blue visible range, which is a relatively lower penetration depth compared to red and NIR light due to absorption and scattering by biological tissues. This implies that red and NIR emissions peak at 695 nm and 800 nm of Tm^{3+} inside the "optical window" are more suited for deep tissue imaging than those of the visible UC emissions of Er^{3+} and Ho^{3+} ions.[24] However, Tm^{3+} ions often display the dominating blue fluorescence that peaks at 485 nm in most host materials.[25,26] It is required to create a technique for adjusting the upconversion emission of Tm^{3+}-doped UC luminous materials to increase the red and NIR emission for possible biological applications. Generally, UC efficiency for blue emission is much lower than that of green and red. The absorption of 975 nm photons by Tm^{3+} ions is low. However, the Yb^{3+} ion is an excellent sensitizer, effectively absorbing pump light and transferring absorbed energy to coactivators.

In this work, we detail the synthesis, structural characterization, and in-depth optical evaluation of $Na_5Y(MoO_4)_4$ phosphors co-doped with Yb^{3+} and Tm^{3+} ions. The doping levels ($0.01Tm^{3+}/0.15Yb^{3+}$) were meticulously optimized through preliminary studies to achieve the maximum emission intensity at 975 nm near-infrared (NIR) excitation. We thoroughly examined the effects of these dopants on upconversion luminescence, temperature-dependent fluorescence properties, and photothermal conversion efficiency. Particular emphasis was placed on assessing the material's suitability for multifunctional applications, including high-sensitivity optical thermometry using fluorescence intensity ratio (FIR) techniques, effective NIR-driven photothermal conversion, and deep-tissue *in vivo* imaging, capitalizing on its emission within the biological transparency window.

2. Experimental setup

2.1. Synthesis

The NYMO compounds co-doped with Tm^{3+}/Yb^{3+} were synthesized using the Pechini sol–gel technique.[27] The nanoluminescent materials were prepared using several commercially available chemicals, including $Y(NO_3)_3\cdot 6H_2O$, $(NH_4)_6Mo_7O_{24}\cdot 4H_2O$, $NaNO_3$, NaOH, $Tm(NO_3)_3\cdot 5H_2O$, and $Yb(NO_3)_3\cdot 5H_2O$. To initiate the synthesis, all the precursors were combined in an Erlenmeyer flask and stirred with a magnetic stirrer at 70 °C. Citric acid was subsequently added, resulting in a color shift from green to blue. The mixture was continuously stirred and heated to 80 °C until it underwent hydrolysis, forming a sol and eventually transitioning into a gel. The gel was then calcined by annealing at 800 °C to generate the final product, which was then refined for analytical tests.

2.2. Characterization techniques

X-ray diffraction (XRD) patterns were obtained using a Bruker Advance diffractometer equipped with a Cu $K\alpha_1$ ($\lambda = 1.5406$ Å) radiation source. Measurements were conducted in the 2θ range of 5°–75° with a step size of 0.02°. The morphology of the synthesized samples was analyzed using a Zeiss Supra 55VP FEG-TEM and a Bruker XFlash 5030 detector. Temporal decay profiles were recorded using a 200 MHz LeCroy WS424 oscilloscope coupled with a Hamamatsu R928 photomultiplier tube (PMT). The system was driven by a 10 Hz EKSPLA/NT342/3/UVE pulsed laser (OPO system, 10 ns pulse width). The temperature-dependent luminescence measurements were conducted by placing the as-prepared samples into a Linkam THMS600 heating stage. An Avantes high-resolution CCD detector was used to acquire the photoluminescence (PL) spectra at 975 nm excitation from a Spectra Physics 3900S tunable Ti:sapphire laser. Temperature-dependent emission measurements were taken at 5 K intervals in the range of 298–388 K. For deep-tissue penetration studies, the NYMO:$0.01Tm^{3+}/0.15Yb^{3+}$ nanophosphor was excited at 975 nm using the Ti:sapphire laser (3900S, Spectra Physics) pumped by a Millenia Prime laser (Millenia 15sJSPG). The sub-tissue penetration depths and spatial resolutions achievable with the nanoparticles were investigated using a double-beam fluorescence microscope.

3. Results and discussion

3.1. Crystal structure and morphological characterization

Fig. S1 shows the X-ray diffraction (XRD) patterns for the NYMO matrix when codoped with Tm^{3+}/Yb^{3+} ions. The diffraction peaks obtained from all samples closely matched the standard positions identified for the NYMO standard chart (JCPDS #82-2368),[28] which confirms that doping with rare earth ions did not alter their phase structure. This indicates that the synthesized phosphors have retained a single-phase composition. The

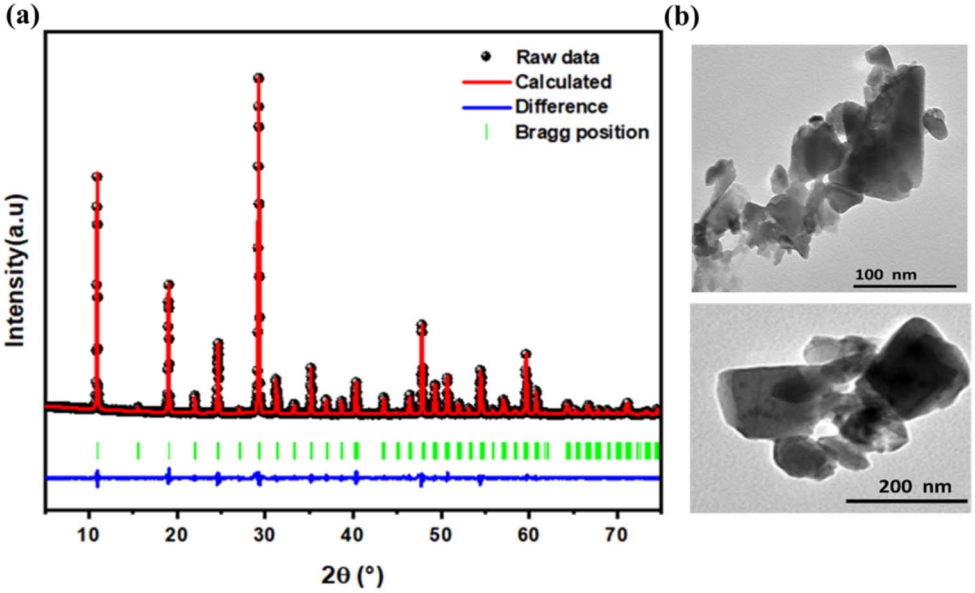

Fig. 1 (a) Rietveld refinement of XRD patterns. (b) TEM images for the NYMO:0.01Tm^{3+}/0.15Yb^{3+} sample.

Rietveld structure refinement of the NYMO:0.01Tm^{3+}/0.15Yb^{3+} phosphor, conducted using the FullProf Suite software, is presented in Fig. 1a. We performed the Rietveld refinement analysis on Tm^{3+}/Yb^{3+}-co-doped NYMO samples to enhance visualization of the crystal structure. The refinement results, obtained with the FullProf Suite, demonstrate a strong agreement between the calculated and experimentally observed diffraction profiles.

Table S1 presents the structural parameters obtained from Rietveld refinement of the samples, which were used to determine their crystal structures. Fig. 1a shows the diffraction patterns of the sample, which were used to confirm the phase purity of the synthesized materials. The sample was found to be single-phase, as no additional diffraction peaks were observed. This indicates that the incorporation of Tm^{3+} and Yb^{3+} ions did not result in the formation of secondary phases. While this observation supports the successful incorporation of dopant ions into the NYMO lattice, definitive evidence of their substitution for Y^{3+} ions requires further structural or spectroscopic analysis. To validate this substitution, the percentage difference in the ionic radius (D_r) between Tm^{3+}, Yb^{3+}, and the host Y^{3+} ion was calculated:[29]

$$D_r(\%) = \frac{R_s(CN) - R_d(CN)}{R_s(CN)} \times 100\% \quad (1)$$

Here, CN is the coordination number, R_s (CN) is the radius of the cations in the framework, and R_d (CN) is the radius of the dopant. The ionic radius difference (D_r) should not exceed 30%. The ionic radii of Y^{3+}, Yb^{3+} and Tm^{3+} are 0.9 Å, 0.985 Å and 0.994 Å, respectively. The coordination number of both ions is 8. The D_r values in NYMO activated with Tm^{3+}/Yb^{3+} were found to be 9.44% and 10.44%, indicating that both Tm^{3+} and Yb^{3+} successfully substitute the lattice positions of the Y^{3+} sites.[30]

The morphology of the samples co-doped with Tm^{3+}/Yb^{3+} in NYMO phosphors was observed by transmission electron microscopy (TEM), as shown in Fig. 1b. The images reveal noticeable grain aggregation, with particle sizes predominantly ranging from 100 to 200 nm.

3.2. Optical characterization

3.2.1. Up-conversion luminescent properties. Fig. 2a shows the emission spectrum of the NYMO:0.01Tm^{3+}/0.15Yb^{3+} phosphor under 975 nm excitation, from which we can observe the typical characteristic emission peaks of Tm^{3+} ions from the f–f transitions ranging from 400 to 900 nm. All the bands identified are attributed to the intra-configuration 4f–4f radiative transition of Tm^{3+}: $^1G_4 \rightarrow {}^3H_6$ (477 nm) and $^3H_4 \rightarrow {}^3H_6$ (796 nm).[31,32] The excited states of Tm^{3+} (UC emitter) are mainly pumped by UC energy transfer processes when the absorbed NIR-light by Yb^{3+} ions, acting as a sensitizer, transfer their energy to the neighboring Tm^{3+}.

A CIE chromaticity diagram of NYMO:0.01Tm^{3+}/0.15Yb^{3+} is shown in Fig. 2b, which shows that NYMO:Tm^{3+}/Yb^{3+} has a CIE coordinate of (0.2194, 0.2161) and is in the blue region, indicating that it can emit bright blue light. Moreover, from the recorded optical images, we can witness the brilliant red emission when the finished products were treated with the UV light.[33] To further study the color behavior of the created red light, the following equation was used to assess its color purity:[34]

$$CP = \sqrt{\frac{(x - x_{eei})^2 + (y - y_{ee})^2}{(x_d - x_{ee})^2 + (y_d + y_{ee})^2}} \quad (2)$$

Here, $(x, y) = (0.2194, 0.2161)$, $(x_{ee}, y_{ee}) = (0.310, 0.316)$ and $(x_d, y_d) = (0.677, 0.322)$ are attributed to the CIE coordinates of the evaluated phosphors (NYMO: white illumination, and dominant wavelength (796 nm)).[35] Thus, the color purity of the emitted blue light from the developed phosphors was 93.8%, indicating that the Tm^{3+}/Yb^{3+}-activated NYMO phosphors can

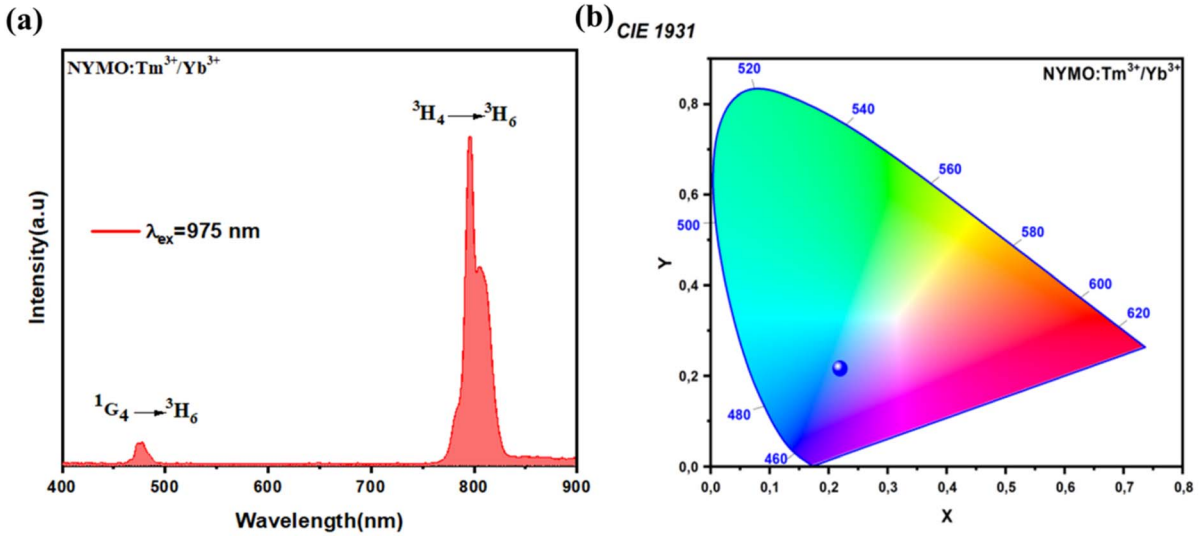

Fig. 2 (a) PL. (b) Chromaticity diagram of NYMO phosphors codoped with 0.01Tm^{3+}/0.15Yb^{3+} excited at λ_{ex} = 975 nm.

produce high-quality blue light and are suitable for lighting applications.

3.2.2. Mechanisms of up conversion emission. Fig. S2a illustrates the time-dependent behavior of blue and near-infrared (NIR) upconversion (UC) emissions under pulsed 975 nm excitation. The decay curves exhibit a notable rising component, suggesting the presence of UC energy transfer processes that facilitate population of the emitting energy levels.[36]

The influence of pump power on UC luminosity was examined at various powers. Fig. S2b shows the log–log curves derived according to the formula $I_{UC} = P^n$, where n is the number of photons needed for the UC process, P is the power at 975 nm, and I_{UC} is the emission intensity.[37] The formula fit indicates that the slope n values of the emission bands at 477 and 796 nm were 2.38 and 1.21, respectively. This indicates that the blue emission band at 477 nm is due to the three-photon absorption UC process, while the red emission is due to the two-photon absorption UC process.[38]

To further comprehend the energy transfer (ET) process, the ET mechanism in NYMO:0.01Tm^{3+}/0.15Yb^{3+} is presented in Fig. 3. Initially, using a 975 nm pump, Yb^{3+} ions with a higher absorption cross section are stimulated from the $^2F_{7/2}$ state to the $^2F_{5/2}$ state *via* ground-state absorption. These ions subsequently relax non-radiatively to the $^2F_{7/2}$ state, delivering energy to the adjacent Tm^{3+} ions.[39] The energy obtained excites the Tm^{3+} from the $^3H_6$ state to the $^3H_5$ state, and this process may be defined as the ET1 process: $^2F_{5/2}(Yb^{3+}) + {}^3H_6(Tm^{3+}) \rightarrow {}^2F_{7/2}(Yb^{3+}) + {}^3H_5\ (Tm^{3+})$. At this stage, part of the non-radiative Tm^{3+} relaxes to the $^3F_4$ state and subsequently proceeds to absorb photons to the $^3F_{2,3}$ states. This process is termed the ET2 process: $^2F_{5/2}\ (Yb^{3+}) + {}^3F_4\ (Tm^{3+}) \rightarrow {}^2F_{7/2}\ (Yb^{3+}) + {}^3F_{2,3}\ (Tm^{3+})$. It then delivers energy to the $^3H_6$ state in the form of a faint red glow. The other Tm^{3+} ions in the $^3H_5$ state continually absorb photons and pump them to the $^1G_4$ state. It then relaxes to the $^3F_4$ state.[40,41] The intense red light at 796 nm is generated by the continuous non-radiative relaxation of Tm^{3+} in the $^3F_{2,3}$ states. In this process, the Tm^{3+} ions, which have relaxed to the $^3H_4$ state, absorb photons again and are pushed to the $^1G_4$ state by the ET3 process: $^2F_{5/2}(Yb^{3+}) + {}^3H_4(Tm^{3+}) \rightarrow {}^2F^{7/2}(Yb^{3+}) + {}^1G_4(Tm^{3+})$. It then emits energy back to the $^3H_6$ state in a nonradiative relaxation mode, resulting in blue light at 477 nm.[42]

3.3. Temperature-dependent UC property of NYMO:Tm^{3+}/Yb^{3+}

The material investigated as an optical temperature sensor was evaluated by analyzing the temperature-dependent luminescence spectra. The results are illustrated in Fig. 4a. In order to determine the thermometric parameters, we studied the following two transitions of Tm^{3+} ions. Following the UC

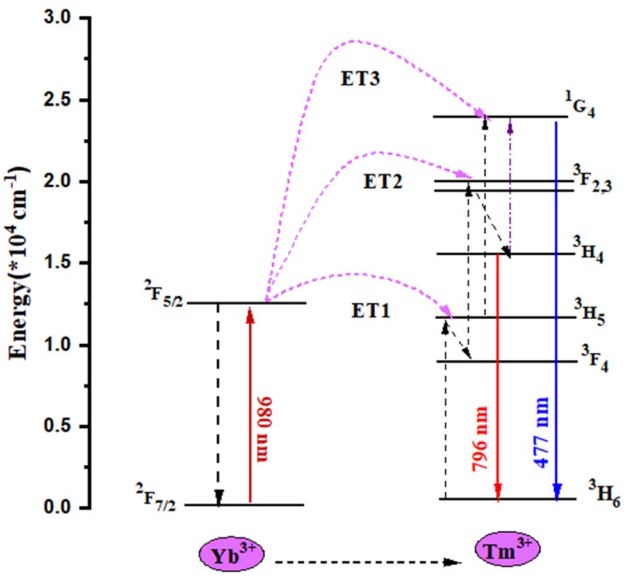

Fig. 3 Proposed energy transfer mechanism of NYMO:0.01Tm^{3+}/0.15Yb^{3+}.

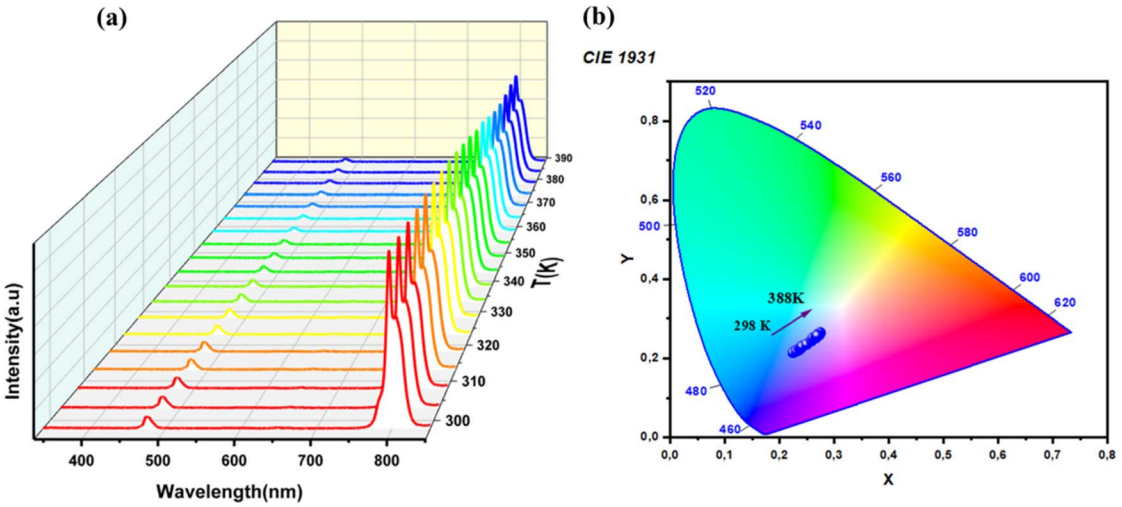

Fig. 4 (a) UC emission spectra. (b) CIE chromaticity diagram of Yb^{3+}/Tm^{3+}-doped NYMO under 975 nm excitation at various temperatures from 298 to 388 K.

emission studies of NYMO:0.01Tm^{3+}/0.15Yb^{3+} samples, the Yb^{3+}-codoped samples were investigated for UC emission. Since Yb^{3+}, when excited at 975 nm, is effective in producing the UC emission from Tm^{3+} ions, it was chosen as a sensitizer.[43,44]

As the temperature increases from 298 K to 388 K, the upconversion (UC) emission intensity of the NYMO:0.01Tm^{3+}/0.15Yb^{3+} nanoparticles decreases for the $^1G_4 \rightarrow {}^3H_6$ and $^3H_4 \rightarrow {}^3H_6$ transitions of Tm^{3+} ions. This temperature-dependent reduction in Tm^{3+} luminescence alters the color of the NYMO luminophores under 975 nm excitation. Specifically, the emitted color shifts noticeably from blue to pink as the temperature rises from 298 K to 388 K, accompanied by a continuous decrease in brightness. This color tunability, driven by temperature control, highlights the robust stability of Tm^{3+} ions. These findings suggest that temperature can be qualitatively assessed through the observed thermal bleaching behavior, as depicted in Fig. 4b.

In order to determine the temperature-dependent UC behavior of the converted particles, the FIR (I_{796}/I_{477}) values as a function of T are shown in Fig. 5a. The blue emission band at 477 nm in the fluorescent sample corresponds to the Tm^{3+} energy level transition to $^1G_4$. The $^1G_4$ level and the other level ($^3H_4$) are not TCELs, and the electronic population does not follow a Boltzmann distribution, and hence temperature cannot be calculated using this rule. Therefore, a polynomial eqn (3) with fitting constants A1, A2, A3 and A4 is utilized to fit the FIR value of non-TCELs.[45–47] The experimental data were fitted to a straight line, yielding a good linear fit (R^2 value is 0.999).

$$\mathrm{FIR} = A_1 + A_2 \times T + A_3 \times T^2 + A_4 \times T^3 \quad (3)$$

In practice, absolute and relative sensitivities are often used to quantify the temperature measurement behaviour of thermometers, which can be defined mathematically as follows.[48,49]

$$S_a = \left|\frac{\delta \mathrm{FIR}}{\delta T}\right| \quad S_r = \frac{1}{\mathrm{FIR}}\left|\frac{\delta \mathrm{FIR}}{\delta T}\right| \quad (4)$$

The values of S_a and S_r can be evaluated as a function of the various un-coupled energy levels. Fig. 5b shows the variations in sensitivity parameters (S_a and S_r) as a function of temperature between 298 K and 388 K. It is worthwhile to study a co-doped sample for optical thermometry because of the availability of different NTCLs with the same or different dopants, which can offer more possibilities for tuning the sensitivity of the thermometer. Moreover, Fig. 5b provides an overview of the estimated maximum value of the sensitivity parameters for each case. It shows that for the selected pair of NTCLs (796/477 nm), the NYMO sample has the highest relative sensitivity ($S_{r\ max} = 2.05\%\ K^{-1}$) in the physiological temperature range.

As illustrated in Fig. S3, the experimental temperature uncertainty was determined by measuring 100 spectra at 298 K under similar conditions since the sensor operation additionally depends on the temperature resolution estimate. Temperature resolution values show typically a Gaussian distribution around ambient temperature.[50,51] In this case, the standard deviation is 0.54 K. To give a complete comparison with the previously published FIR thermometers, the thermal sensing features of different materials, including sensitivity and operating spectral range, are presented in Table 1. The sensitivity of NYMO is substantially greater than that of previously reported similar materials, suggesting that it is an excellent candidate material for luminous temperature monitoring.

To test the accuracy of the temperature measuring technique, the thermometric parameters (FIR values) were regularly measured. This was done by cycling the sample between low and high temperatures. The results are shown in Fig. S4. Repeatability (R) was defined as the average of the absolute differences between the repeated measurements.

$$R_p(100\%) = \left(1 - \frac{\max\left|M_i(T)_c - M(T)_c\right|}{\mathrm{FIR}_c}\right) \times 100 \quad (5)$$

$M_i(T)_c$ is the measurement parameter (FIR or band centroid) in the ith cycle and $M(T)_c$ is the average value of $M(T)$ over seven cycles. The FIR values showed reversible variations in response to

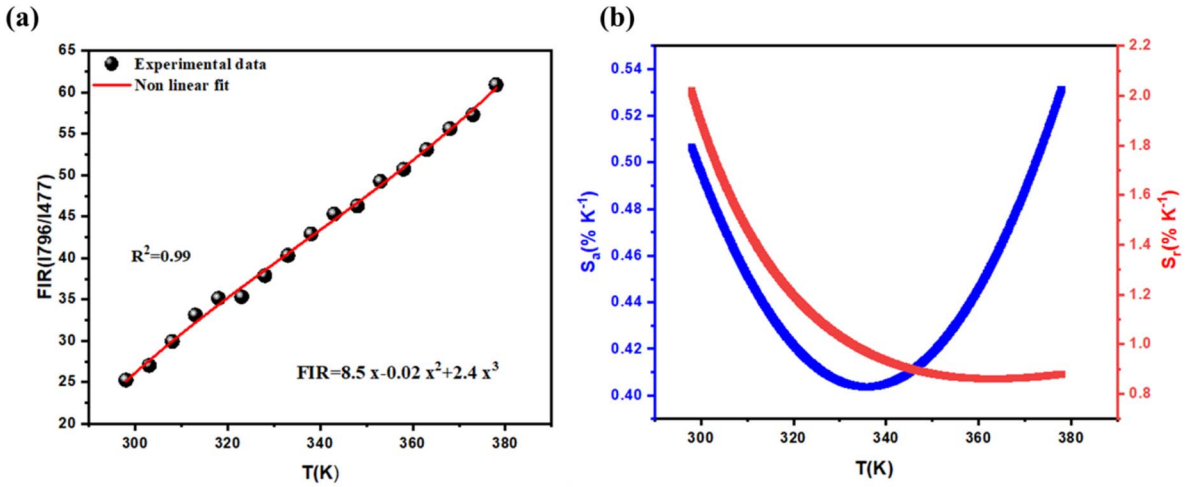

Fig. 5 (a) Experimental data and the fitted line of the FIR. (b) Curves of relative sensitivity, S_r, and absolute sensitivity, S_a, of NYMO co-doped Yb^{3+}/Tm^{3+} in the temperature range of 298–388 K.

Table 1 Comparison of the sensitivity (S_r) of varied materials

Samples	Temperature range (K)	$S_{r\ max}$ (% K^{-1})	Ref.
Tm^{3+}:Y_2O_3	303–753	0.35	52
Yb^{3+}/Tm^{3+}:Sr_2GdF_7	293–563	1.97	53
Yb^{3+}/Tm^{3+}:Y_2O_3	303–573	1.5	54
Yb^{3+}/Tm^{3+}:NaY_2F_7	307–567	1.63	55
Yb^{3+}/Tm^{3+}:$GdVO_4$	297–673	0.87	56
Yb^{3+}/Tm^{3+}:$NaBiF_4$	303–443	1.1	57
Yb^{3+}/Tm^{3+}:$Y_2Ti_2O_7$	300–400	0.87	58
Yb^{3+}/Tm^{3+}:$Na_3GdV_2O_8$	298–565	2.01	59
Yb^{3+}/Tm^{3+}:$LiNbO_3$	400–773	0.7	60
Yb^{3+}/Tm^{3+}:NLMO	300–650	1.16	61
Yb^{3+}/Tm^{3+}:PbF_2 GC	300–700	0.30	62
Yb^{3+}/Tm^{3+}:$NaYF_4$	300–510	1.53	63
Yb^{3+}/Tm^{3+}:NYMO	298–388	2.05	This work

temperature, with all observed FIRs above 98% throughout the tested temperatures. This result demonstrated the high reproducibility and dependability of the thermometric methods used.

3.4. Photothermal conversion performance of Tm^{3+}/Yb^{3+} codoped NYMO phosphors

To evaluate the photothermal conversion performance of the NYMO:0.01Tm^{3+}/0.15Yb^{3+} nanophosphor under 975 nm laser excitation, upconversion (UC) emission spectra were measured across a range of excitation power densities (90.8 to 194.9 W cm^{-2}), as shown in Fig. 6a. Variations in the population distribution of the energy levels result in differing intensity changes for the $^1G_4 \rightarrow {}^3H_6$ and $^3H_4 \rightarrow {}^3H_6$ transitions of Tm^{3+} ions within the sample. This differential intensity variation causes a shift in the fluorescence intensity ratio (FIR), defined as I_{796}/I_{477}, with increasing excitation power density. The FIR as a function of excitation power density is plotted in Fig. 6b, revealing a gradual increase in FIR as the power density rises from 90.8 to 194.9 W cm^{-2}. This trend indicates a corresponding rise in the sample's internal temperature with higher laser power, as illustrated in Fig. 6c. A greater change in FIR values signifies more pronounced heating of the material.[64,65]

The temperature increase in the NYMO:0.01Tm^{3+}/0.15Yb^{3+} phosphor is primarily due to energy absorption by the crystalline powder, which is then dissipated as heat *via* nonradiative processes. This thermal energy propagates from the crystal, raising the temperature of the surrounding volume. Concurrently, enhanced electron–phonon interactions further contribute to heating within the crystal, with these interactions becoming more significant at higher temperatures. These findings highlight the efficient conversion of NIR laser excitation power density into heat by the Tm^{3+}/Yb^{3+} co-doped NYMO phosphor, positioning it as a promising material for photothermal therapy applications.[66,67]

3.5. Investigation of the depth of penetration under tissue

To assess the suitability of the NYMO:0.01Tm^{3+}/0.15Yb^{3+} nanophosphor for biological experiments, a vertical setup was designed to excite the sample using a method similar to those reported in the literature.[68–70]

Using the experimental setup schematically illustrated in Fig. 7a and described in detail in the Experimental section, we investigated the optical attenuation experienced by the two emission bands of NYMO:0.01Tm^{3+}/0.15Yb^{3+} nanoparticles (NPs). This configuration enabled us to quantify the progressive attenuation of Tm^{3+} luminescence as it propagates through a blood layer of controlled thickness. The NPs were excited with a 975 nm laser, and the resulting upconversion emission was collected by a microscope objective positioned opposite the sample. Blood, known for its high absorption and scattering coefficients in the NIR-I region, is widely used as a tissue-mimicking phantom to approximate the optical response of human skin.[71,72] Its extinction coefficient spectrum, measured using a Lambda 1050 PerkinElmer double-beam absorption spectrometer, is shown in Fig. 7b.

Fig. 7c presents the measured emission intensity of Tm^{3+}/Yb^{3+} co-doped NYMO NPs (emission at 796 nm) as a function of

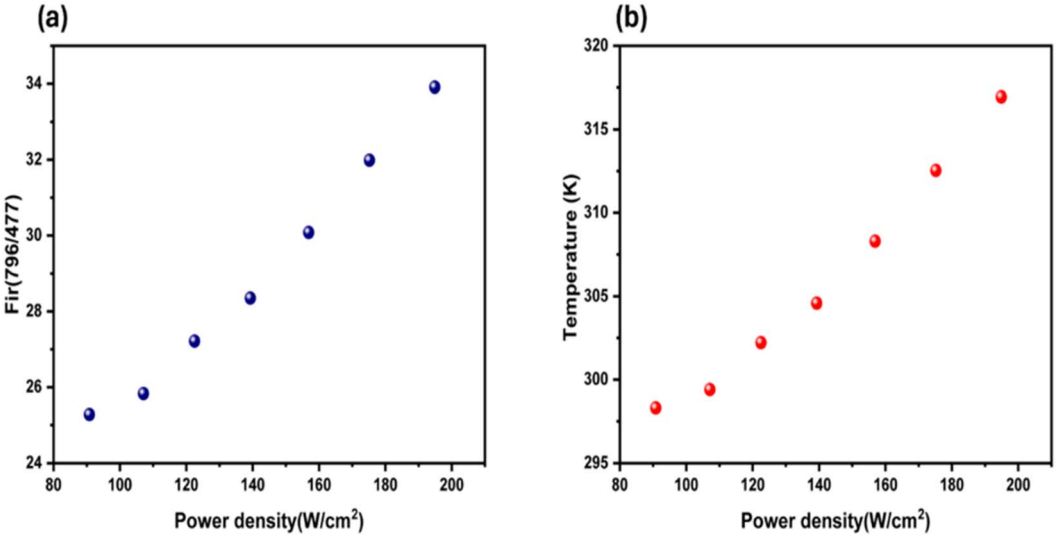

Fig. 6 Power dependence of NYMO:0.01Tm^{3+}/0.15Yb^{3+} ions. (a) The fitted line of FIR (796/477) and (b) calibration temperature.

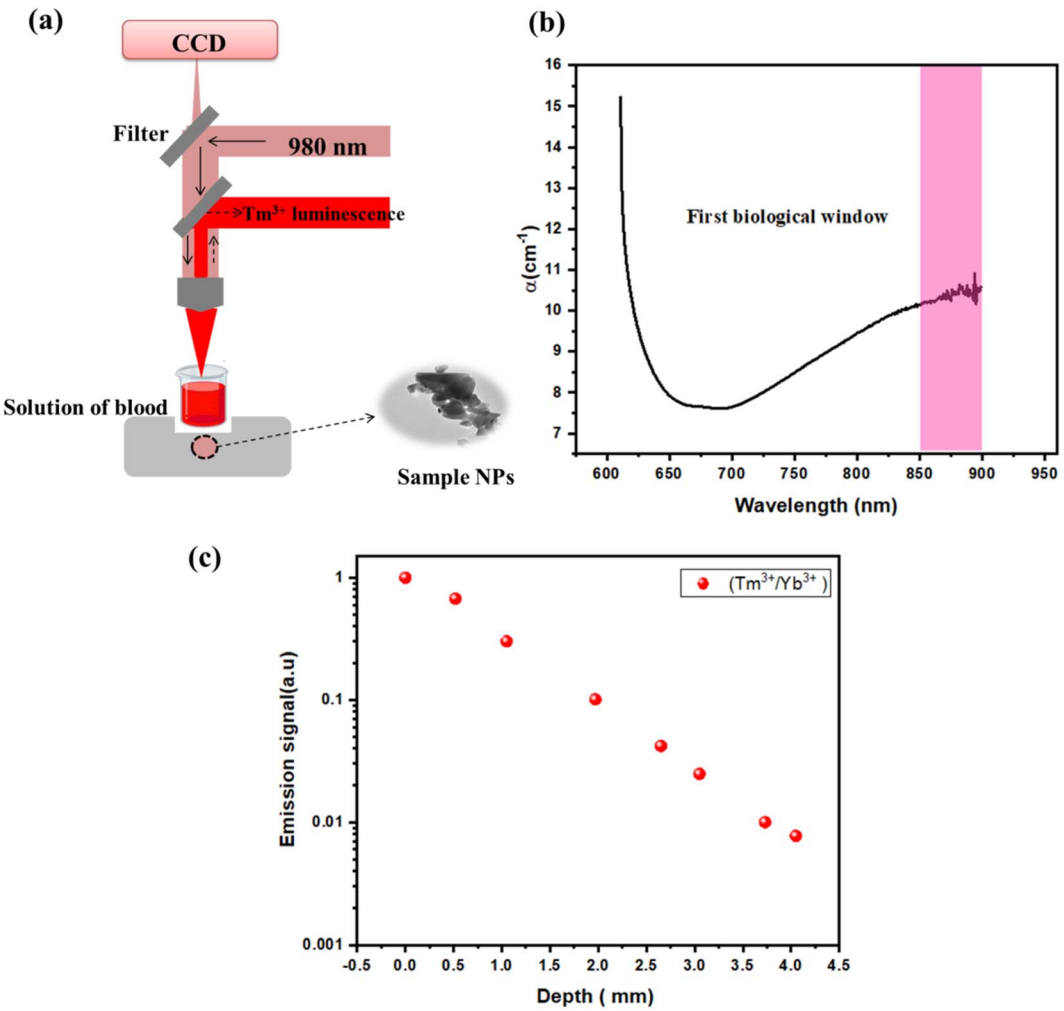

Fig. 7 (a) Schematic representation of the experimental setup for the determination of the penetration depth of two photon-excited NYMO nanoparticles. (b) Wavelength dependence of blood extinction coefficient. (c) Intensity of photon-excited luminescence emitted by Tm^{3+} nanoparticles: NYMO as a function of blood thickness under 975 nm excitation.

phantom thickness. As expected, the luminescence signal decreases monotonically with increasing depth, consistent with attenuation dominated by absorption and scattering processes.[73] The attenuation profile was quantitatively analyzed, allowing us to estimate the depth at which the signal drops to the detectable limit under our measurement conditions. Based on this analysis, the effective *in vitro* penetration depth for the 796 nm emission is approximately 4 mm in the blood phantom. It should be noted that this value represents an inferred penetration depth from the attenuation curve rather than a direct imaging demonstration. Nevertheless, the observed attenuation behavior aligns well with reported NIR propagation characteristics in biological tissues and confirms that the Tm^{3+}-based emission exhibits enhanced transmission through strongly scattering media. These results highlight the potential of NYMO:0.01Tm^{3+}/0.15Yb^{3+} nanoparticles for applications requiring improved light penetration in biological environments.

4. Conclusion

In this study, we successfully synthesized Tm^{3+}/Yb^{3+}-co-doped NYMO nanoparticles using the sol–gel method and comprehensively characterized their structural, morphological, and luminescent properties. Under a 975 nm laser excitation, the upconversion (UC) emission spectra displayed two distinct bands at 477 nm and 796 nm, corresponding to the $^1G_4 \rightarrow {}^3F_6$ and $^3H_4 \rightarrow {}^3H_6$ transitions of Tm^{3+} ions, respectively. By applying the fluorescence intensity ratio (FIR) method between these emission bands, the nanoparticles exhibited a maximum relative sensitivity (S_r) of 2.05% K^{-1} at 298 K and a maximum absolute sensitivity (S_a) of 0.53% K^{-1} at 388 K, demonstrating their potential for high-precision optical thermometry. To evaluate photothermal conversion performance, the UC emission spectra were measured across a range of excitation power densities (90.8–194.9 W cm^{-2}). The observed variation in emission intensity was attributed to changes in the population distribution among energy levels, resulting in a gradual increase in FIR (I_{796}/I_{477}) with increasing excitation power. This indicates a rise in internal temperature driven by laser-induced energy absorption and subsequent nonradiative heat dissipation, further amplified by enhanced electron–phonon interactions at elevated temperatures. Additionally, under 975 nm excitation, the near-infrared (NIR) emission from the NYMO nanoparticles remained detectable at tissue depths of up to 4 mm, confirming their exceptional tissue penetration capabilities. Operating within the biological optical window, these Tm^{3+}-sensitized NYMO nanoparticles enable effective deep-tissue imaging and enhanced detection of subtle biological signals. In conclusion, the Tm^{3+}/Yb^{3+} co-doped NYMO nanoparticles exhibit outstanding optical sensitivity, efficient photothermal conversion, and robust tissue penetration, positioning them as highly promising candidates for integrated applications in optical temperature sensing, photothermal therapy, and deep-tissue *in vivo* imaging.

Conflicts of interest

There are no conflicts to declare.

Data availability

All data underlying the results are available as part of the article and no additional source data are required.

Supplementary information (SI) is available. See DOI: https://doi.org/10.1039/d5ra08947f.

References

1 I. E. Kolesnikov, *J. Lumin.*, 2018, **204**, 506–512.
2 K. Saidi, M. Yangui, C. H. Álvarez, M. Dammak, I. R. M. Benenzuela and M. Runowski, *ACS Appl. Mater. Interfaces*, 2024, **16**, 19137–19149.
3 X. Ai, J. Mu and B. Xing, *Theranostics*, 2016, **6**, 2439–2457.
4 S. Lal, S. E. Clare and N. J. Halas, *Acc. Chem. Res.*, 2008, **41**, 1842–1851.
5 L. Liu, S. Wang, B. Zhao, P. Pei, Y. Fan, X. Li and F. Zhang, *Angew. Chem., Int. Ed.*, 2018, **57**, 7518–7522.
6 Y. Liu, X. Meng and W. Bu, *Coord. Chem. Rev.*, 2019, **379**, 82–98.
7 D. Jaque, *et al.*, *Nanoscale*, 2014, **6**, 9494–9530.
8 X. Huang, W. Zhang, G. Guan, G. Song, R. Zou and J. Hu, *Acc. Chem. Res.*, 2017, **50**, 2529–2538.
9 X. Meng, B. Zhang, Y. Yi, H. Cheng, B. Wang, Y. Liu, T. Gong, W. Yang, Y. Yao, H. Wang and W. Bu, *Nano Lett.*, 2020, **20**, 2522–2529.
10 D. M. Yang, P. A. Ma, Z. Y. Hou, Z. Y. Cheng, C. X. Li and J. Lin, *Chem. Soc. Rev.*, 2015, **44**, 1416–1448.
11 B. Yan and J.-H. Wu, *Mater. Chem. Phys.*, 2009, **116**, 67–71.
12 S. Piovesana, D. M. S. Schietroma and M. Bella, *Angew. Chem., Int. Ed.*, 2011, **50**, 6216–6232.
13 E. Hemmer, P. Acosta-Mora, J. Méndez-Ramos and S. Fischer, *J. Mater. Chem. B*, 2017, **5**, 4365–4392.
14 B. del Rosal, E. Ximendes, U. Rocha and D. Jaque, *Adv. Opt. Mater.*, 2017, **5**, 1600508.
15 C. D. Brites, S. Balabhadra and L. D. Carlos, *Adv. Opt. Mater.*, 2018, 1801239.
16 K. Okabe, R. Sakaguchi, B. Shi and S. Kiyonaka, *Eur. J. Physiol.*, 2018, **470**, 717–731.
17 Y. Bahrouni, I. Kachou, K. Saidi, T. Kallel, M. Dammak, I. Mediavilla and J. Jiménez, *Mater. Adv.*, 2025, **6**, 1307–1318.
18 I. Kachou, K. Saidi, C. Hernandez-Alvarez, M. Dammak and I. R. Martın, *Mater. Adv.*, 2024, **5**, 8280–8293.
19 M. Fhoula, K. Saidi, C. H. Álvarez, K. S. Carracedo, M. Dammak and I. R. Martín, *J. Alloys Compd.*, 2024, **979**, 173537.
20 G. Chen, J. Shen, T. Y. Ohulchanskyy, N. J. Patel, A. Kutikov, Z. Li, *et al.*, *ACS Nano*, 2012, **6**, 8280–8287.
21 H. Qiu, G. Chen, R. Fan, L. Yang, C. Liu, S. Hao, *et al.*, *Nanoscale*, 2014, **6**, 753–757.
22 M. Quintanilla, I. X. Cantarelli, M. Pedroni, A. Speghini and F. Vetrone, *J. Mater. Chem. C*, 2015, **3**, 3108–3113.
23 Z. E. A. A. Taleb, K. Saïdi, M. Dammak, D. Przybylska and T. Grzyb, *Dalton Trans.*, 2023, **52**, 4954–4963.
24 S. Chen, W. Song, J. Cao, F. Hu and H. Guo, *J. Alloys Compd.*, 2020, **825**, 154011.

25 P. Haro-gonzález, I. R. Martín, N. E. Capuj and F. Lahoz, *Opt. Mater.*, 2010, **32**, 1349–1351.
26 W. Chen, J. Cao, F. Hu, R. Wei, L. Chen and H. Guo, *J. Alloys Compd.*, 2018, **735**, 2544–2550.
27 C. S. Lim, V. Atuchin, A. Aleksandrovsky and M. Molokeev, *J. Am. Ceram. Soc.*, 2015, **98**(10), 3223–3230.
28 C. Wei, J. Zhang, Z. Sun, J. Ran, S. Lia, S. Zhu, C. Jiang, Y. Wen and X. Ran, *J. Alloys Compd.*, 2024, **991**, 174428.
29 T. Sonali, V. Chauhan, P. C. Pandey and C. Shivakumara, *ACS Appl. Opt. Mater.*, 2024, **2**, 41–56.
30 X. Wu, X. Zhao, Q. Ren, L. Du, M. Pei and O. Hai, *Ceram. Int.*, 2022, **48**, 18793–18802.
31 B. Klimesz, R. Lisiecki and W. Ryba-Romanowski, *J. Alloys Compd.*, 2020, **823**, 153753.
32 H. Lv, P. Du, W. Li and L. Luo, *ACS Sustain. Chem. Eng.*, 2022, **10**, 2450–2460.
33 K. Dharendra, A. Roy, A. Dwivedi, A. K. Rai, S. B. Rai and D. Kumar, *Mater. Res. Bull.*, 2021, **139**, 111280.
34 M. Wang, S. Ding, C. Zhang, H. Ren, Y. Zou, X. Tang and Q. Zhang, *Ceram. Int.*, 2023, **49**, 37661–37669.
35 E. Hasabeldaim, H. C. Swart and R. E. Kroon, *Phys. B*, 2023, **671**, 415417.
36 Y. Chen, G. Chen, X. Liu, J. Xu, X. Zhou, T. Yang, C. Yuan and C. Zhou, *Opt. Mater.*, 2018, **81**, 78–83.
37 M. Z. Yang, Y. Sui, S. P. Wang, X. J. Wang, Y. Q. Sheng, Z. G. Zhang, T. Q. Lu and W. F. Liu, *Chem. Phys. Lett.*, 2010, **492**, 40–43.
38 Q. Min, W. Bian, Y. Qi, W. Lu, X. Yu, X. Xu, D. Zhou and J. Qiu, *J. Alloys Compd.*, 2017, **728**, 1037–1042.
39 R. Lisiecki, J. Komar, M. Berkowski and W. Ryba-Romanowski, *J. Lumin.*, 2019, **216**, 116721.
40 W. Ge, M. Xu, J. Shi, J. Zhu and Y. Li, *Chem. Eng. J.*, 2020, **391**, 123546.
41 X. Zhao, H. Suo, Z. Zhang, G. Zhang and C. Guo, *Ceram. Int.*, 2020, **46**, 3183–3189.
42 F. R. O. Silva, N. B. Lima, W. K. Yoshito, A. H. A. Bressiani and L. Gomes, *J. Lumin.*, 2017, **187**, 240–246.
43 J. Xing, F. Shang and G. Chen, *J. Non-Cryst. Solids*, 2021, **569**, 120989.
44 K. Li, Q. Zhanga, G. Bai, S. Fana, J. Zhanga and L. Hua, *J. Alloys Compd.*, 2010, **504**, 573–578.
45 I. Kachou, K. Saidi, R. Salhi and M. Dammak, *RSC Adv.*, 2022, **12**(12), 7529–7539.
46 W. Gao, W. Ge, J. Shi, X. Chen and Y. Li, *J. Solid State Chem.*, 2021, **297**, 122063.
47 S. Liu, J. Cui, J. Jia, J. Fu, W. You, Q. Zeng, Y. Yang and X. Ye, *Ceram. Int.*, 2019, **45**, 1–10.
48 R. Li, G. Wei, Z. Wang, Y. Wang, J. Li, S. He, L. Li, H. Suo, W. Ding and P. Li, *Laser Photonics Rev.*, 2023, **17**, 2200589.
49 K. Saidi, C. Hernandez-Alvarez, M. Runowski, M. Dammak and I. R. Martín, *Dalton Trans.*, 2023, 14904–14916.
50 C. D. S. Brites, P. P. Lima, N. J. O. Silva, A. Millan, V. S. Amaral, F. Palacio and L. D. Carlos, *Nanoscale*, 2012, **4**, 4799–4829.
51 S. Liu, H. Ming, J. Cui, S. Liu, W. You, X. Ye, Y. Yang, H. Nie and R. Wang, *J. Phys. Chem. C*, 2018, **122**, 16289–16303.
52 D. Y. Li, Y. X. Wang, X. R. Zhang, *et al.*, *Opt. Commun.*, 2012, **285**, 1925–1928.
53 W. Chen, J. Cao, F. Hu, R. Wei, L. Chen and H. Guo, *J. Alloys Compd.*, 2018, **735**, 2544–2550.
54 G. Chen, R. Lei, H. Wang, F. Huang, S. Zhao and S. Xu, *Opt. Mater.*, 2018, **77**, 233–239.
55 S. Chen, W. Song, J. Cao, F. Hu and H. Guo, *J. Alloys Compd.*, 2020, **825**, 154011.
56 O. A. Savchuk, J. J. Carvajal, C. Cascales, J. Massons, M. Aguilo and F. Díaz, *J. Mater. Chem. C*, 2016, **4**(27), 6602–6613.
57 H. Tian, L. Dou and L. Wu, *Opt. Mater.*, 2020, **99**, 109544.
58 X. Tu, J. Xu, M. Li, T. Xie, R. Lei, H. Wang and S. Xu, *Mater. Res. Bull.*, 2019, **112**, 77–83.
59 Y. Bahrouni, I. Kachou, K. Saidi, C. Hernández-Álv, M. Dammak and I. R. Martínc, *J. Mater. Chem. C*, 2025, 13415–13425.
60 L. Xing, R. Ao, Y. Liu and W. Yang, *Spectrochim. Acta, Part A*, 2019, **222**, 117159.
61 S. Tomar, N. Kumar, M. Vaibhav, C. K. Kumar and C. Shivakumara, *J. Phys. Chem. C*, 2024, **128**, 10159–10174.
62 W. Xu, X. Y. Gao, L. J. Zheng, Z. G. Zhang and W. W. Cao, *Sens. Actuators, B*, 2012, **173**, 250–253.
63 A. F. Pereira, K. U. Kumar, W. F. Silva, W. Q. Santos, D. Jaque and C. Jacinto, *Sens. Actuators, B*, 2015, **213**, 65–71.
64 P. Zhang, X. Wang, S. Zhao, X. Wang, R. Lei, L. Huang and S. Xu, *J. Phys. Chem. C*, 2023, **127**, 12770–12778.
65 S. Xiang, B. Chen, J. Zhang, X. Li, J. Sun, H. Zheng, Z. Wu, H. Zhong, H. Yu and H. Xia, *Opt. Mater. Express*, 2014, **4**, 1966–1980.
66 V. K. Kikhomirov, K. Driesen, V. D. Rodriguez, P. Gredin, M. Mortier and V. V. Moshchalkov, *Opt. Express*, 2009, **17**, 11794–11798.
67 R. K. Verma and S. B. Rai, *J. Quant. Spectrosc. Radiat. Transfer*, 2012, **13**, 1594–1600.
68 U. Rocha, K. U. Kumar, C. Jacinto, I. Villa, F. Sanz-Rodríguez, M. D. C. Iglesias De La Cruz, A. Juarranz, E. Carrasco, F. C. J. M. Van Veggel, E. Bovero and J. G. Solé, *Small*, 2014, **10**, 1141–1154.
69 U. Rocha, C. Jacinto Da Silva, W. Ferreira Silva, I. Guedes, A. Benayas, L. M. Maestro, M. Acosta Elias, E. Bovero, F. C. J. M. Van Veggel, J. A. García Solé and D. Jaque, *ACS Nano*, 2013, **7**, 1188–1199.
70 L. Zhou, R. Wang, C. Yao, X. M. Li, C. L. Wang, X. Y. Zhang, C. J. Xu, A. J. Zeng, D. Y. Zhao and F. Zhang, *Nat. Commun.*, 2015, **6**, 6938–6948.
71 M. A. Hernandez-Rodríguez, A. D. Lozano-Gorrín, I. R. Martín, U. R. Rodríguez-Mendoza and V. Lavín, *Sens. Actuators, B*, 2017, 970–976.
72 X. Zhao, H. Suo, Z. Zhang and C. Guo, *Ceram. Int.*, 2019, 21910–21916.
73 N. N. Dong, M. Pedroni, F. Piccinelli, G. Conti, A. Sbarbati, J. E. R. Hernández, L. M. Maestro, M. C. I.-d. Cruz, F. S. Rodriguez, A. Juarranz, F. Chen, F. Vetrone, J. A. Capobianco, J. G. Solé, M. Bettinelli, D. Jaque and A. Speghini, *ACS Nano*, 2011, **5**, 8665–8671.